PHYSICAL REVIEW B **95**, 134435 (2017)

Combining microscopic and macroscopic probes to untangle the single-ion anisotropy and exchange energies in an $S = 1$ quantum antiferromagnet

Jamie Brambleby,[1,*] Jamie L. Manson,[2,3,†] Paul A. Goddard,[1] Matthew B. Stone,[4] Roger D. Johnson,[5,6] Pascal Manuel,[6]
Jacqueline A. Villa,[2] Craig M. Brown,[3] Helen Lu,[7] Shalinee Chikara,[7] Vivien Zapf,[7] Saul H. Lapidus,[8] Rebecca Scatena,[9]
Piero Macchi,[9] Yu-sheng Chen,[10] Lai-Chin Wu,[10] and John Singleton[5,7,‡]

[1]*Department of Physics, University of Warwick, Gibbet Hill Road, Coventry CV4 7AL, United Kingdom*
[2]*Department of Chemistry and Biochemistry, Eastern Washington University, Cheney, Washington 99004, USA*
[3]*NIST Center for Neutron Research, National Institute of Standards and Technology, Gaithersburg, Maryland 20899, USA*
[4]*Quantum Condensed Matter Division, Oak Ridge National Laboratory, Oak Ridge, Tennessee 37831, USA*
[5]*University of Oxford, Department of Physics, The Clarendon Laboratory, Parks Road, Oxford, OX1 3PU, United Kingdom*
[6]*ISIS Pulsed Neutron Source, STFC Rutherford Appleton Laboratory, Didcot, Oxfordshire OX11 0QX, United Kingdom*
[7]*National High Magnetic Field Laboratory, MS-E536, Los Alamos National Laboratory, Los Alamos, New Mexico 87545, USA*
[8]*X-ray Sciences Division, Advanced Photon Source, Argonne National Laboratory, Argonne, Illinois 60439, USA*
[9]*Department of Chemistry and Biochemistry, University of Bern, 3012 Bern, Switzerland*
[10]*ChemMatCARS, Advanced Photon Source, Argonne National Laboratory, Argonne, Illinois 60439, USA*

(Received 21 November 2016; revised manuscript received 12 February 2017; published 20 April 2017)

The magnetic ground state of the quasi-one-dimensional spin-1 antiferromagnetic chain is sensitive to the relative sizes of the single-ion anisotropy (D) and the intrachain (J) and interchain (J') exchange interactions. The ratios D/J and J'/J dictate the material's placement in one of three competing phases: a Haldane gapped phase, a quantum paramagnet, and an XY-ordered state, with a quantum critical point at their junction. We have identified [Ni(HF$_2$)(pyz)$_2$]SbF$_6$, where pyz = pyrazine, as a rare candidate in which this behavior can be explored in detail. Combining neutron scattering (elastic and inelastic) in applied magnetic fields of up to 10 tesla and magnetization measurements in fields of up to 60 tesla with numerical modeling of experimental observables, we are able to obtain accurate values of all of the parameters of the Hamiltonian [$D = 13.3(1)$ K, $J = 10.4(3)$ K, and $J' = 1.4(2)$ K], despite the polycrystalline nature of the sample. Density-functional theory calculations result in similar couplings ($J = 9.2$ K, $J' = 1.8$ K) and predict that the majority of the total spin population resides on the Ni(II) ion, while the remaining spin density is delocalized over both ligand types. The general procedures outlined in this paper permit phase boundaries and quantum-critical points to be explored in anisotropic systems for which single crystals are as yet unavailable.

DOI: 10.1103/PhysRevB.95.134435

I. INTRODUCTION

The possibility of arranging interacting magnetic moments in chains or planes has excited theorists and experimentalists alike for many years. The pioneering work by Kosterlitz and Thouless on properties of the XY model (a two-dimensional vector spin model that possesses U(1) or circular symmetry) [1,2], and by Haldane on integer-spin chains [3,4], has had far-reaching implications, culminating in the award of the 2016 Nobel Prize in Physics [5]. More recently, interest in predicting and controlling the magnetic ground state of $S = 1$ quantum magnets has been fueled by the realization of a myriad of magnetic phases in a series of metal-organic coordination compounds. This includes the observation of field-induced Bose-Einstein condensation in NiCl$_2$-4SC(NH$_2$)$_2$ [6–8], as well as the development of a Haldane phase in both [Ni(C$_2$H$_8$N$_2$)$_2$NO$_2$]ClO$_4$ [9] and [Ni(HF$_2$)(3-Clpy)$_4$]BF$_4$ (Clpy = C$_5$H$_4$NCl = chloropyridine) [10–12]. Ground-state diversity is attributable to the interplay between the single-ion anisotropy (D) and Heisenberg spin-exchange interactions in these materials, which are determined (in part) by the lattice geometry [12]. The flexibility offered by the crystal structures of quasi-one-dimensional (Q1D) coordination polymers renders them ideal systems to advance our understanding of the quantum-critical phenomena associated with $S = 1$ systems.

The magnetic ground state of a Q1D $S = 1$ antiferromagnet (AFM) is particularly sensitive to both the precise nature of D and its strength compared to J, the intrachain Heisenberg spin-exchange interaction [10]. The Hamiltonian in a magnetic field ($B \approx \mu_0 H$) is

$$\mathcal{H} = \sum_{\langle i,j\rangle} J\mathbf{S}_i.\mathbf{S}_j + \sum_{\langle i,j'\rangle} J'\mathbf{S}_i.\mathbf{S}_{j'} + \sum_i \left[D\left(S_i^z\right)^2 + g\mu_{\mathrm{B}}\mathbf{S}_i.\mathbf{B}\right], \quad (1)$$

where $\mathbf{S}$ is the spin of each ion (i), $\langle i,j\rangle$ denotes a sum over nearest neighbors, J' is the strength of the interchain interaction, a primed index in the summation describes the interaction with a nearest neighbor in an adjacent chain, and g is the isotropic g factor.

Unlike classical systems, ideal $S = 1$ chains ($J' = 0$) are vulnerable to strong quantum fluctuations [11], which can have a profound influence on the magnetic ground state and act to suppress long-range order. Quantum Monte-Carlo (QMC) simulations predict that for easy-plane anisotropy, a Haldane ground state gives way to quantum paramagnetism (QP) as

---

[*] j.d.brambleby@warwick.ac.uk
[†] jmanson@ewu.edu
[‡] jsingle@lanl.gov

the D/J ratio increases. On the other hand, the effects of J' are to alleviate the quantum disorder and induce an XY-AFM ordered phase (i.e., an AFM with the antialigned spins lying in a two-dimensional plane) [10]. A phase diagram illustrating these phenomena will be described in Sec. III and Fig. 12. (If $D = 0$, the ordered phase will be a Néel-type AFM [10].) The three magnetic phases are expected to converge at a quantum critical point (QCP) [13], located at $D/J = 0.97$ for purely 1D chains (Fig. 12) [12]. Therefore, the ability to measure J, J', and D precisely, in addition to obtaining an unambiguous experimental determination of the magnetic ground state in real systems, is a crucial step towards testing the theoretical predictions of quantum phenomena in Q1D $S = 1$ chains. However, as we now describe, this has proved difficult in the case of polycrystalline samples, particularly for those systems in which the exchange and anisotropy energies are similar in magnitude. A major challenge is the time required to hone synthetic methods sufficiently to obtain single crystals large enough for many measurement techniques. Therefore it is frequently the newest, most exciting families of materials that are most difficult to characterize.

In the absence of a magnetic field and strong spin-exchange interactions, systems described by Eq. (1) are dominated by single-ion anisotropy. This energy term acts to remove the spin-microstate degeneracy of paramagnetic Ni(II) ions ($m_s = 0, \pm 1$) and is dependent upon both the metal-ligand electronic structure and the spin-density distribution. For hexa-coordinated Ni(II) complexes, this zero-field splitting (ZFS) of energy levels can result in a singlet ($D > 0$) or doublet ground state with D-values that have been found to span the range $-32 \leqslant D \leqslant 20$ K [14,15]. So long as the Ni$\cdots$Ni spin-exchange interactions are weak, the D value in complexes of this type may be characterized by magnetic susceptibility, magnetization, and heat capacity measurements. However, a reliable estimation of both the size *and* sign of D in polycrystalline samples is only possible via these techniques if one can apply magnetic fields of a sufficient strength to significantly align the spins [16]. Electron-spin resonance (ESR) is also frequently used to determine the anisotropy and can work well for powdered samples but only provided the frequency-field combination that matches the ZFS can be achieved.

For exchange-coupled systems, the sensitivity of bulk thermodynamic probes to the spin correlations further complicates the extraction of a unique value for the single-ion anisotropy. A resolution to this problem is offered by microscopic probes such as inelastic neutron scattering (INS), which is well suited to distinguish the effects of spin-exchange interactions from those of single-ion anisotropy. The origin of spin excitations (spin-wave or crystal-field levels) may be discriminated by their wave-vector (**Q**) and energy-transfer (E) dependence [17]. In the past, successful treatment of INS data has relied on D-only models (ignoring J), as found in high-nuclearity Mn(III) complexes [18,19], J-only models (ignoring D) in some Co(II) complexes [20–22], or $J > D$ as determined in Q1D $MnCl_2(urea)_2$ [23]. To the best of our knowledge, analysis of powder INS spectra has not been successfully tested in multiparameter systems where $D \approx J$ until now. Without INS data, density-functional theory (DFT) is often implemented to validate thermodynamic parameters according to a prescribed Hamiltonian [such as Eq. (1)]. The results, however, are sensitive to the basis set employed and require experimental support if one is to have confidence in the outcome [24–26].

Here we describe a complete experimental procedure to determine the H,T phase diagram and all of the parameters of the spin Hamiltonian of $[Ni(HF_2)(pyz)_2]SbF_6$ (pyz = pyrazine = $C_4H_4N_2$), despite the lack of suitable single crystals. This material is composed of linear HF_2^- pillars that mediate an intrachain Ni$\cdots$Ni exchange coupling (J), while bridging pyrazine ligands provide four equivalent interactions (J') to neighboring chains [27,28]. The material enters an AFM ordered phase below 12.2 K and exhibits $D/J \approx 1$, along with a predicted $J'/J \approx 0.1$ (from DFT calculations) [27]. It therefore provides a rare opportunity to study the magnetic properties of a system close to the three competing Q1D ground states.

Below the ordering temperature, elastic neutron scattering of $[Ni(HF_2)(pyz)_2]SbF_6$ reveals that the zero-field magnetic structure is that of a 3D XY-AFM ground state. Based on this result, the anisotropic critical field observed in powder magnetization measurements can then be interpreted within an easy-plane, mean-field picture to initially estimate values of $D = 15(1)$ K and $n\langle J\rangle = 22.4(2)$ K (n = number of magnetic nearest neighbors and $\langle J\rangle$ = average spin-exchange interaction strength). Applying Eq. (1) in SPINW [29], we model powder INS spin-wave spectra to deconvolute the two distinct AFM contributions to $n\langle J\rangle$ to yield $J = 10.4(3)$ K and $J' = 1.4(2)$ K that we assign to Ni-FHF-Ni and Ni-pyz-Ni interactions, respectively. Given these parameters, we find good agreement with the predictions of QMC calculations for the low-temperature phase, and this result is used to explain the form of the field-temperature phase diagram revealed by heat capacity and magnetization measurements. We compare these parameters to those obtained from low-field magnetic susceptibility measurements and demonstrate the shortcomings in modeling these data in the absence of other information. Lastly, we provide a detailed analysis of the spin-density distribution and exchange-coupling constants as predicted by periodic DFT calculations. Full details of the experimental methods and theoretical calculations and simulations can be found in the Supplemental Material [30].

II. RESULTS AND DISCUSSION

A. Low-temperature chemical and magnetic structure

1. Microcrystal x-ray diffraction

The 15 K structure (Fig. 1) of $[Ni(HF_2)(pyz)_2]SbF_6$ was solved in the tetragonal space group $P4/nmm$ based on the single-crystal x-ray diffraction data. Whilst the microcrystals were suitable for a synchrotron x-ray structural study, they were much too small for single-crystal thermodynamic and neutron-scattering measurements [30]. (Full details of the structural refinement are given in Table S1 in the Supplemental Material. Selected bond lengths and bond angles can be found in Table S2 [30].) Each Ni(II) ion is axially coordinated to two F atoms at a distance of 2.076(1) Å. These F atoms belong to bridging HF_2^- ligands that form one-dimensional linear Ni-FHF-Ni chains along the c axis with respective F$\cdots$F and Ni$\cdots$Ni separations of 2.276(1) Å and 6.4292(1) Å. These

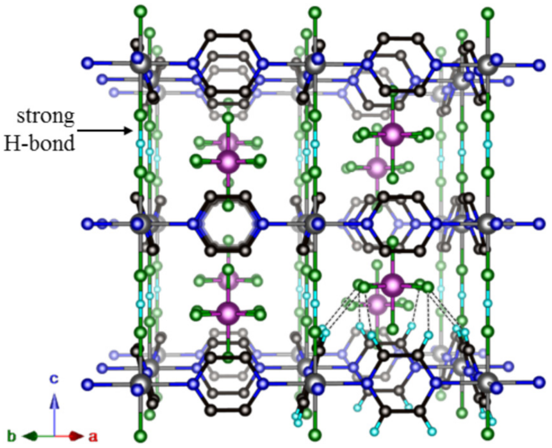

FIG. 1. $[Ni(HF_2)(pyz)_2]SbF_6$ structure determined by microcrystal x-ray diffraction ($T = 15$ K). The material is a polymeric metal-organic framework including interstitial SbF_6^- ions. Each Sb atom occupies the fourfold rotation axis that lies parallel to the c direction but the centroid of the SbF_6^- ion is displaced about 0.6 Å from the ideal body-centered position. For clarity, only the lower right quadrant depicts the weak hydrogen bonds that exist between pyz ligands and the SbF_6^- ion ($H \cdots F = 2.478$ Å; dashed lines). Ni = gray, H = cyan, F = green, C = black, N = blue, Sb = purple.

linkages mediate an intrachain interaction through σ-bond magnetic coupling as established by experiment and DFT (see below). Pyrazine ligands join the Ni(II) ions [$\mathrm{Ni}-\mathrm{N} = 2.098(1)$ Å] along the [110] and $[1\bar{1}0]$ directions to produce two-dimensional (2D) square sheets in the ab plane, which have equal Ni-Ni separations of 6.9860(2) Å and provide the interchain interactions. The slight difference in Ni-F and Ni-N bond lengths results in a weakly compressed octahedral NiN_4F_2 coordination environment. *Trans*-coordinated pyz ligands are counter-rotated and tilt away from the NiN_4 plane by 73.04(4)°. The ordering of the pyz ligands in $[Ni(HF_2)(pyz)_2]SbF_6$ contrasts the twofold positional disorder encountered in the related quasi-two-dimensional (Q2D) layered coordination polymers $NiZ_2(pyz)_2$ ($Z =$ Cl, Br, I, NCO), which crystallize in the $I4/mmm$ space group [31,32]. The structurally related material, $Ni(NCS)_2(pyz)_2$, has monoclinic symmetry and no apparent pyz disorder [31].

Interstitial sites within the $[Ni(HF_2)(pyz)_2]^+$ framework are occupied by charge-compensating SbF_6^- ions. Significant close contacts of 2.478 Å exist between pyrazine H atoms and equatorial Fs from the SbF_6^- [Fig. 1, dashed lines]. These weak $C\text{-}H \cdots F$ hydrogen bonds probably constrain the pyz ligands to the observed configuration and are unlikely to contribute to significant additional magnetic exchange mechanisms.

2. *Elastic neutron scattering*

The chemical structure of $[Ni(HF_2)(pyz\text{-}d_4)_2]SbF_6$ was refined at 1.5 and 20 K using Rietveld analysis as implemented in FULLPROF [33]. Structural parameters derived from the microcrystal x-ray study of the hydrogenated phase were used as initial input. As anticipated, the deuterated material was isostructural to the hydrogenated phase, and the magnetic properties of the two compounds were found to be very similar based on susceptibility measurements. (Unit-cell parameters derived from neutron scattering can be found in Table S3 in the Supplemental Material, whereas Table S2 compares bond lengths and bond angles provided by the x-ray and neutron experiments [30]).

Examining the difference in scattered neutron intensity obtained at 1.5 and 20 K [Fig. 2(a)] reveals three distinct Bragg peaks at approximately 3.94 Å, 4.19 Å, and 7.85 Å that do not overlap any nuclear peaks. These are attributed to long-range AFM order of Ni(II) moments in the material. Indexing of the superlattice peak at 7.85 Å requires doubling of the chemical unit cell along the c axis. This indicates that the intrachain interaction along the HF_2^- bridge is AFM in nature, as was also found to be the case in the isostructural Cu(II) and Co(II) congeners [27]. Thus, the magnetic unit cell corresponds to a propagation vector $\mathbf{k} = (0,0,\frac{1}{2})$ referenced to reciprocal lattice vectors based on the chemical unit cell.

Symmetry analysis using ISODISTORT [34] gave four irreducible representations, which correspond to candidate magnetic structures with either ferromagnetic (FM) or antiferromagnetic nearest-neighbor magnetic moments in the ab plane. In either case, the magnetic moments may be oriented exactly parallel or perpendicular to the tetragonal c axis. The magnetic moments separated along the c axis are aligned antiparallel, consistent with the magnetic propagation vector $(0,0,\frac{1}{2})$. Structure-factor calculations demonstrated that the FM and AFM ab-plane structures have opposite reflection conditions, allowing the FM case to be ruled out. Two spin directions are then unique by symmetry:

(i) spins orthogonal to the crystallographic c axis; or
(ii) spins parallel to the c axis.

These two scenarios were tested through refinement of the respective magnetic structure models against the diffraction data. It was found that only scenario (i) quantitatively predicts the relative intensities of all of the measured magnetic Bragg peaks, as is clearly shown in Fig. 2(a) and corroborated by the respective agreement factors (R_{mag}) of 5.89 % and 18.6% for scenario (i) and (ii). General comparison between calculated (F_c^2) and observed (F_o^2) structure factors for preferred configuration (i) show very good correlation (see Table S4 [30]). The powder-averaged data were found to be insensitive to the global moment orientation within the ab plane. We therefore conclude that the ordered phase of $[Ni(HF_2)(pyz)_2]SbF_6$ is consistent with the 3D XY-AFM ground state depicted in Fig. 2(b).

At $T = 1.5$ K, the experimentally determined Ni(II) magnetic moment has a magnitude of $2.03(7)\mu_{\mathrm{B}}$, which is the same within errors as the full moment expected for an $S = 1$ ion, $gS\mu_{\mathrm{B}} = 2.08\mu_{\mathrm{B}}$, given the published [27] powder-average g factor. This observed full moment precludes strong quantum fluctuations in the ground state which were prominent in the Q2D Heisenberg $S = \frac{1}{2}$ Cu(II) analog, for which a reduced ordered moment of $0.6(1)\mu_{\mathrm{B}}$ was found [35]. The differing results can be attributed to the smaller spin-quantum number and strong quantum fluctuations, the significantly smaller J'/J ratio, and the lack of single-ion anisotropy in the copper material.

Data plotted in Fig. 2(c) were obtained by fitting the ordered moment to each measured diffraction pattern. The resulting fit of these data to the power law [36], $M(T) = M(0)[1 - T/T_{\mathrm{c}}]^{\beta}$, yielded $T_{\mathrm{c}} = 12.13(7)$ K and $\beta = 0.141(1)$. For most systems the critical region in which

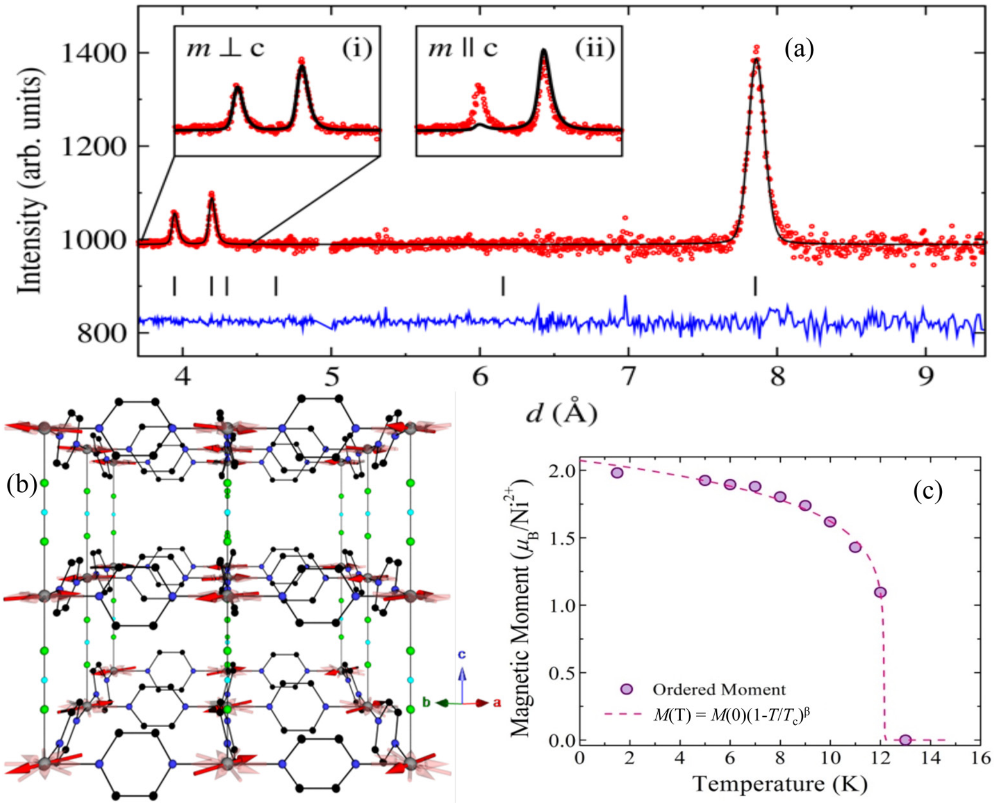

FIG. 2. Elastic neutron scattering data. (a) Magnetic diffraction pattern (red points) for $[\mathrm{Ni(HF_2)(pyz\text{-}d_4)_2}]\mathrm{SbF_6}$ obtained by subtracting data collected at 20 K from that collected at 1.5 K (see Supplemental Material [30]). The fitted spectrum (black line) has the Ni(II) moment lying in the *ab* plane. Bragg peaks are indicated by ticks and the blue line is the difference between the data and the fit. The insets show a comparison of the model calculated with the moments perpendicular (i) or parallel (ii) to the *c* axis. (b) Zero-field magnetic structure (omitting pyz Hs and $\mathrm{SbF_6^-}$). Collinear XY-ordered Ni(II) magnetic moment vectors are indicated by red arrows. The translucent red arrows demonstrate uncertainty in the global orientation of the magnetic moments in the *ab* plane. (c) T dependence of the ordered Ni(II) magnetic moment. The power law fit (see text) yields $T_c = 12.13(7)$ K and $\beta = 0.141(1)$.

power-law behavior applies is restricted to $1 - T/T_c < 10^{-2}$ [37]. Sparse data in the vicinity of T_c warrants caution in assigning β to a particular model.

3. *Field-dependent heat capacity and susceptibility*

The $H = 0$ heat capacity plotted as C_p/T versus T [Fig. 3(a)] shows a sharp maximum at 12.2(1) K, indicating a transition to long-range order in addition to a sloping background due to the phonon contribution. The data for $T \geqslant 32$ K have been modeled [38] with one Debye and two Einstein phonon modes (the resulting fit parameters are tabulated in Table S5 [30]). The three lattice modes show similar energy scales to those deduced from analogous analysis of the copper [38] and cobalt [35] isomorphs, which results from the shared structure of this family of compounds. Subtracting the phonon heat capacity from the total measured heat capacity of $[\mathrm{Ni(HF_2)(pyz)_2}]\mathrm{SbF_6}$, the magnetic heat capacity shows a broad hump that develops on cooling and precedes a transition to long-range order (Fig. 3). This broad feature corresponds to a significant reduction in the spin entropy for $T > T_c$ (inset) and is likely to result from the combination of two mechanisms that restrict the magnetic degrees of freedom of the system: (i) development of XY anisotropy of the individual Ni(II) moments, as well as (ii) the buildup of AFM spin correlations among neighboring Ni(II) ions dispersed along the Ni-FHF-Ni chains.

For $T \ll T_c$, spin-wave excitations are the dominant contribution to the magnetic heat capacity. The data below 8 K have been represented with a power law T^n, where n has a fitted value of $n = 3.09(3)$. This exponent was previously reported for the total sample heat capacity [27], but the new results specifically exclude contributions to the measurement from the Debye mode. A T^3 dependence of the heat capacity is expected for an AFM ordered system within which the magnetic excitations (magnons) propagate in three dimensions [39], which highlights the need to include the effects of J and J' in the analysis of the spin-wave excitation spectra measured by inelastic neutron scattering (see below).

The field dependence of the heat capacity [$\mu_0 H \leqslant 9$ T, Fig. 3(c)] and the linear susceptibility [$M/\mu_0 H$; $\mu_0 H \leqslant 13$ T, Fig. 3(d)] implies that the transition temperature is suppressed in applied magnetic field, as required for an AFM. The overall field dependence is weak up to 13 T, owing to the large critical fields in this system, and the high-field portion of the phase diagram was explored using pulsed-field magnetization measurements (see below).

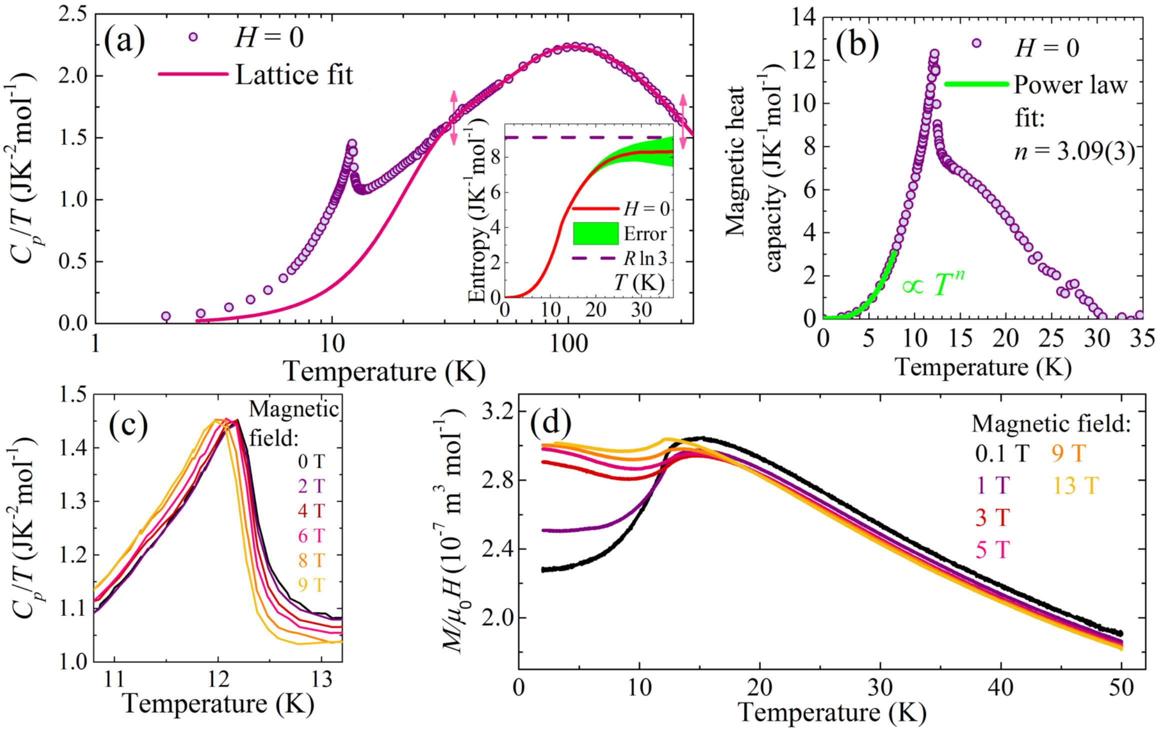

FIG. 3. (a) Ratio of heat capacity to temperature T for [Ni(HF$_2$)(pyz)$_2$]SbF$_6$ (points). Data for $T > 32$ K have been fitted (arrows) to a model of one Debye and two Einstein modes (line). The inset shows the magnetic entropy up to 35 K where it can be seen to approach the expected value of $R\ln 3$ for $S = 1$ ions. (b) Magnetic heat capacity (C_{mag}) exhibits a broad maximum preceding a sharp transition at 12.2(1) K, indicating the onset of long-range order. Data below 8 K were fitted to a power law, T^n, yielding $n = 3.09(3)$. (c) Field dependence of T_c for $0 \leqslant \mu_0 H \leqslant 9$ T. (d) Field-dependent linear susceptibility ($M/\mu_0 H$) versus T, showing a broad maximum, the temperature of which is suppressed by increasing H.

B. Experimental determination of D, J, and J'

1. High-field magnetization

The pulsed-field magnetization of [Ni(HF$_2$)(pyz)$_2$]SbF$_6$ at low temperatures shows a slightly concave rise with increasing field and a broadened approach to saturation [Fig. 4(a)]. Two critical fields are identified at 0.6 K, which correspond to an initial increase and subsequent decrease in dM/dH close to 32 T and the point where dM/d$H \to 0$ near 54 T [Fig. 4(b), arrows]. To interpret the primary features, we adopt a mean-field model for AFM-coupled easy-plane $S = 1$ ions which may be justified based on the ground state determined from elastic neutron scattering (see above). Within this model the saturation field should be anisotropic with an easy plane and a hard axis such that two saturation fields could be observed in the powder data. For fields perpendicular and parallel to the magnetic hard axis, each of these saturation fields (H_{c1} and H_{c2}, respectively) can be calculated using

$$\mu_0 H_{c1} = \frac{2n\langle J\rangle}{g\mu_B} \quad \text{and} \quad \mu_0 H_{c2} = \frac{2(n\langle J\rangle + D)}{g\mu_B}, \tag{2}$$

where n is the number of nearest neighbors for each magnetic ion and $\langle J\rangle$ is an average spin-exchange interaction. In a powder measurement, a decrease in dM/dH starts at H_{c1} once a portion of the sample begins to saturate. Finally, dM/d$H \to 0$ at H_{c2}, where no further increase in the magnetization can occur as all Ni(II) moments are aligned with the magnetic field.

The first critical field, H_{c1} for [Ni(HF$_2$)(pyz)$_2$]SbF$_6$ is easily identified at all $T < 15$ K (Fig. 4). Combining these critical fields with the heat-capacity results (above), the field-temperature phase diagram can be derived (Fig. 5). The phase boundary for fields applied perpendicular to the magnetic hard axis (solid lines) is fitted to the expression

$$T_c(H) = T_c(0)\left[1 - \left(\frac{H}{H_{c1}}\right)^{\alpha_1}\right]^{\beta_1}. \tag{3}$$

Fixing $T_c(0) = 12.2$ K, the resultant fitted parameters are $\mu_0 H_{c1} = 32.0(3)$ T, $\alpha_1 = 4.6(4)$, $\beta_1 = 0.56(4)$.

The temperature evolution of the saturation field for fields parallel to the magnetic hard axis ($\mu_0 H_{c2}$) is more difficult to follow; the dM/dH signal is lowest in this field region and arises from a diminishing proportion of the sample as H_{c2} is approached. In addition, as the temperature increases, the transition to saturation is broadened further. At two of the lowest temperatures, however, the saturation field can be identified and is found to be $\mu_0 H_{c2} = 54(1)$ T at 0.6 K.

Using these critical fields in conjunction with Eqs. (2) and the powder average g value [27] of 2.08, we determine $D = 15(1)$ K and $n\langle J\rangle \equiv 2J + 4J' = 22.4(2)$ K. To decompose $n\langle J\rangle$ into individual J and J' contributions, we appeal to a catalog of related coordination polymers that also contain square [Ni(pyz)$_2$]$^{2+}$ motifs [31,40] (see Table S7 [30]). From this, we glean an average $J' = 0.9(2)$ K. Applying this to [Ni(HF$_2$)(pyz)$_2$]SbF$_6$ leads to $J = 9.4(5)$ K. Therefore, the resultant D/J and J'/J ratios are more than and less than

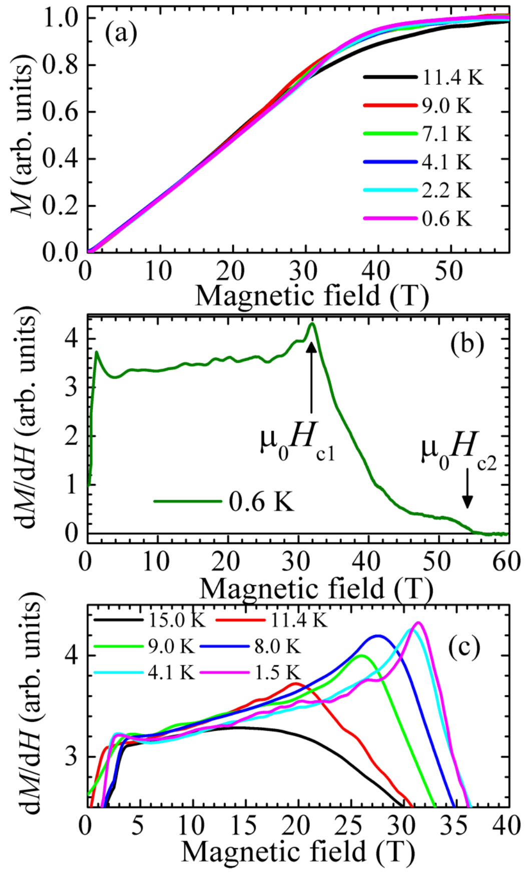

FIG. 4. (a) Magnetization M versus applied magnetic field $\mu_0 H$ for [Ni(HF$_2$)(pyz)$_2$]SbF$_6$ measured in pulsed fields for selected $T \leqslant 15$ K. (b) Differential susceptibility dM/dH versus $\mu_0 H$ for $T = 0.6$ K; H_{c1} and H_{c2} are shown by arrows. (c) Expansion of dM/dH versus $\mu_0 H$ plots for several T, showing how H_{c1} moves to lower fields as T increases.

one, respectively, consistent with a preliminary DFT study [27] used to calculate J'. These parameters are in reasonable agreement with the results of INS measurements and Monte-Carlo simulations detailed below.

Using these results, the form of the phase diagram shown in Fig. 5 can be interpreted. On cooling the sample from room temperature in zero field, the sample moves from a paramagnetic (PM) phase to a region within which the Ni(II) moments develop XY anisotropy (XY-Q1D) and their directions are antiferromagnetically correlated for neighboring ions along the Ni-FHF-Ni chains, with the moments arranged perpendicular to these chains. On cooling further, there is a magnetic phase transition to an ordered state. We assign this to long-range order with XY moments antiferromagnetically and collinearly aligned to their nearest neighbors. Starting from this ordered phase and applying a magnetic field, the system is driven through a field-induced phase transition to a FM-like phase. This occurs for fields bounded by the range $H_{c1} \leqslant H \leqslant H_{c2}$, depending on whether the field is applied perpendicular (H_{c1}) or parallel (H_{c2}) to the z direction. For powder measurements of the magnetization this anisotropy leads to the slow and broad approach toward saturation.

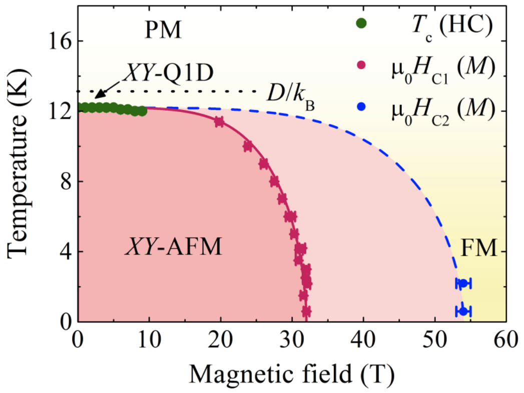

FIG. 5. Field-temperature (H,T) phase diagram for [Ni(HF$_2$)(pyz)$_2$]SbF$_6$, mapped out using data from heat capacity (HC) and pulsed-field magnetization (M) measurements. Here, XY-AFM = long-range XY-AFM order, FM = fully polarized phase, and XY-Q1D is a region where the moments are antiferromagnetically correlated along the chains, with the Ni(II) moments oriented perpendicular to those chains; H_{c1}(H_{c2}) is the field at which the magnetization saturates when field is applied perpendicular (parallel) to the hard axis. The $\mu_0 H_{c1}$ phase boundary (solid line) is modeled using Eq. (3), while the $\mu_0 H_{c2}$ boundary (dashed line) is a guide to the eye. The energy scale of the single-ion anisotropy (D) is indicated by a dotted line for reference.

2. *Inelastic neutron scattering*

Figures 6(a)–6(c) shows the measured powder INS energy-momentum transfer spectrum of [Ni(HF$_2$)(pyz-d$_4$)$_2$]SbF$_6$ in zero field for $T = 1.6, 10$, and 20 K. As the temperature decreases an upper bound of the spectrum appears at a neutron energy transfer ≈3.4 meV. Given that the feature becomes more pronounced on cooling, this T dependence suggests that it is likely associated with spin-wave formation due to long-range magnetic order. The difference between the $T = 1.6$ K and $T = 20$ K spectra [Fig. 6(d)] reveals the magnetic spectrum more clearly, showing a band of excitations that exists below 3.3 meV. Below 1 meV, the high temperature background is large, leading to an over-subtraction of the data. The energy scale, wave-vector, and temperature dependence of the scattering below 1 meV indicate that the large background may be attributed to acoustic phonons that contribute to the scattering intensity at these energies. Furthermore, a small percentage of hydrogen in the sample due to incomplete deuteration could increase the background due to the large incoherent cross section of the ^{1}H isotope. For $T < T_c$, magnetic Bragg peaks along $E = 0$ are evident at $|\mathbf{Q}| \approx 0.8\,\text{Å}^{-1}$, $1.6\,\text{Å}^{-1}$, and $2.0\,\text{Å}^{-1}$ [white arrows in Fig. 6(d)] which is fully consistent with the elastic neutron diffraction patterns.

Figure 7 shows the magnetic-field dependence of the excitation spectrum. For each data set, a $T = 20$ K background measurement at the same applied field was made and subtracted from subsequent field-dependent data. We found these 20 K spectra to give a reasonable representation of the behavior of the paramagnetic phase of our material. The peak in the zero-field spin-wave density-of-states shifts to lower energy transfers as the field increases. The magnetic Bragg peak at

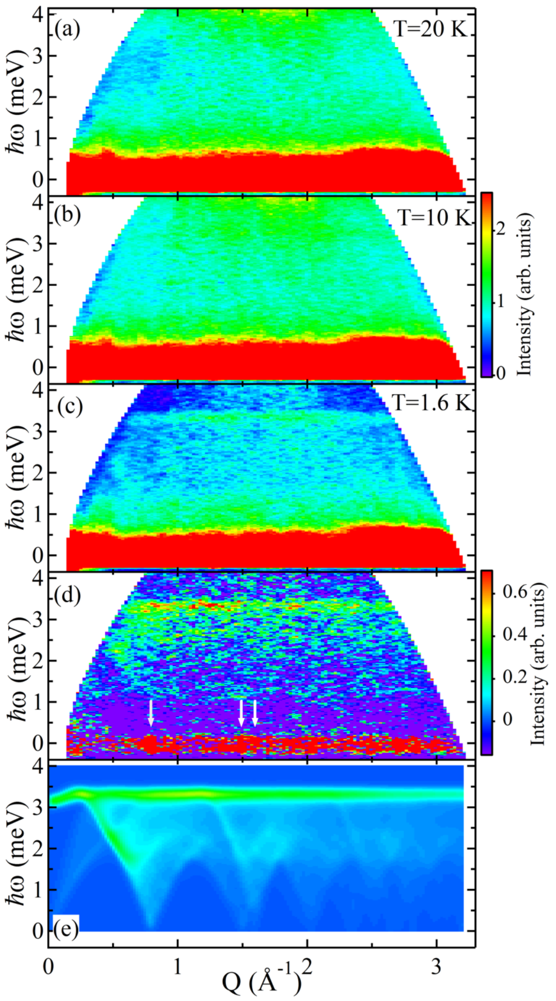

FIG. 6. Intensity contour plots of INS data with no background subtraction for: (a) $T = 20$ K, (b) $T = 10$ K, and (c) $T = 1.6$ K. Panel (d) is the $T = 1.6$ K measurement after subtracting the $T = 20$ K data as a background. The data were binned in units of 0.025 meV and 0.025 Å^{-1} and then smoothed once with a 3×3-bin-sized Gaussian kernel. White arrows in panel (d) highlight the locations of prominent magnetic Bragg peaks as validated by the diffraction experiment on WISH [see Fig. 2(a)]. Panel (e) shows the simulated powder INS spectrum for the parameters $D = 13.3(1)$ K, $J = 10.4(3)$ K, and $J' = 1.4(2)$ K.

$Q = 0.8$ Å^{-1} does not shift with increasing field, indicating that the periodicity of the long-range order does not change with field (see inset of Fig. 8). For $H > 0$, [Figs. 7(b)–7(d)], there is some additional scattering intensity that is present at energies higher than the top of the zero-field spin wave band at 3.4 meV.

Integrating the data from Fig. 7 for momentum transfers in the range 0.8–2.5 Å^{-1}, (Fig. 8) illustrates how the intense portion of the $H = 0$ spin-wave mode at an energy transfer of 3.4 meV softens with applied field. There is also a rise in scattering intensity at higher energy transfers with increasing field indicating that the degeneracy of the spin-wave mode is lifted by the field and a portion of the spectrum is moving to larger energy transfers.

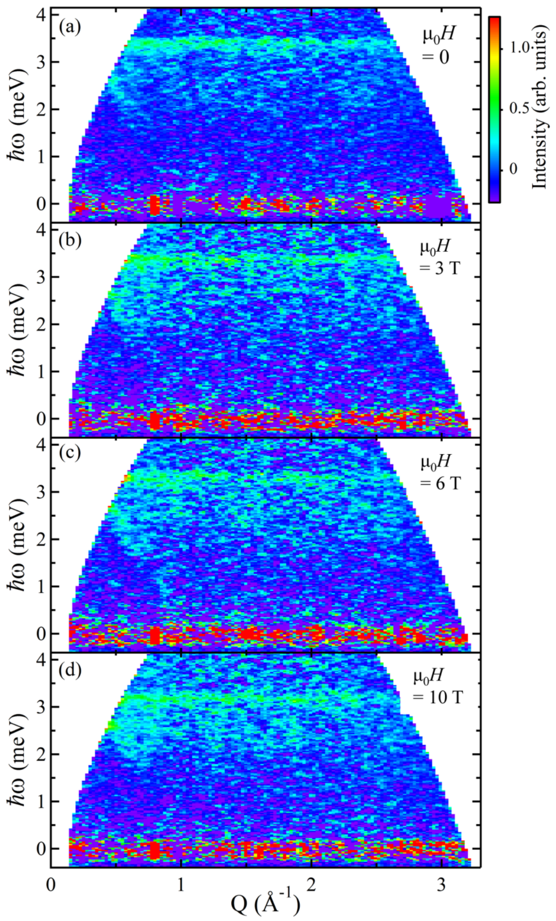

FIG. 7. Background-subtracted magnetic-field dependent INS data obtained at $T = 1.5$ K for (a) $\mu_0 H = 0$, (b) $\mu_0 H = 3$ T, (c) $\mu_0 H = 6$ T, and (d) $\mu_0 H = 10$ T. Data were binned and smoothed in a similar manner to those in Fig. 6. Data measured at $T = 20$ K and at corresponding fields were used as paramagnetic backgrounds for each set taken at 1.5 K.

With the material well within the ordered magnetic phase at $T = 1.6$ K, we modeled the $H = 0$ spectrum shown in Fig. 6(d) using the numerical spin wave calculation package SPINW [29]. We use the aforementioned zero-field magnetic structure as the basis for all subsequent simulations. The exchange interactions J and J' are included in the model as well as the anisotropy term D as described in Eq. (1). A powder-average spin-wave spectrum is calculated for energy transfers between 2 and 4 meV for a large range of values in D, J, and J' parameter space. The limited range of energy transfer was chosen to avoid the lower energy region due to the acoustic-phonon scattering previously described. Each simulated spin-wave spectrum was compared to the measurement and a value of reduced χ^2 was determined for each triplet of energy parameters. Fitting parameters for each simulation included a constant background and an overall multiplicative prefactor to scale the calculated scattering intensity [41,42]. The best-fit parameters were found from the minimum in reduced χ^2. Figure 6(e) shows the final simulated spectrum. The resulting parameters were $D = 13.3(1)$ K, $J = 10.4(3)$ K, and $J' = 1.4(2)$ K, in good agreement with the results estimated from thermodynamic measurements.

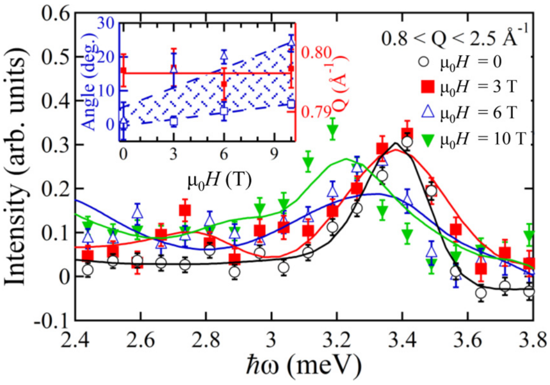

FIG. 8. (Main plot): Background subtracted intensity as a function of energy transfer ($\hbar\omega$) for magnetic fields $\mu_0 H \leqslant 10$ T. The data correspond to those shown in Fig. 7 integrated between 0.8 and 2.5 Å^{-1} in wave-vector transfer. The solid lines correspond to the spin-wave calculations discussed in the text; they use a randomly applied magnetic field orientation. (Inset) The open blue triangles correspond to the field-dependent spin reorientations of the Ni(II) moments using the random-field calculation. The open blue squares correspond to the field-dependent spin reorientations of the Ni(II) moments considering only magnetic field applied along the c axis of the crystal. The shaded area is the range between a linear field-dependent fit to this reorientation angle for each of the models. The solid red squares (right axis) in the inset show the location of the magnetic Bragg peak as a function of H. The solid red line is a fit to a constant value.

Any potential next-next-nearest neighbor Ni-Ni exchange interaction along the a and b axes (i.e., the diagonals of the $[\mathrm{Ni(pyz)_2}]^{2+}$ square plaquettes, see Fig. 1), with a distance of 9.880 Å, would likely be much smaller than J' and ultimately require measurements on single crystals with improved energy resolution to determine accurately.

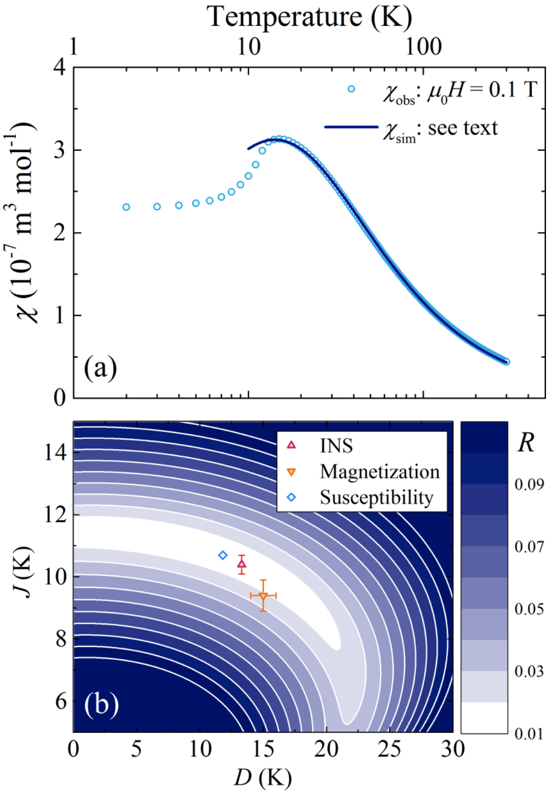

FIG. 9. (a) Magnetic susceptibility χ versus temperature T data for $[\mathrm{Ni(HF_2)(pyz)_2}]\mathrm{SbF_6}$ ($\mu_0 H = 0.1$ T) interpolated to evenly spaced temperatures in the range $2 \leqslant T \leqslant 300$ K, $\Delta T = 1$ K (χ_{obs}, points). (b) Contour plot of the quality factor R in the D, J plane found by comparing the simulated susceptibility [Eqs. (S1) and (S2) [30]] to the measured data (see text for details). The result shows bands of D and J that provide fits to the data of similar quality. The model (χ_{sim}) that yields the minimum value of R (diamond) is displayed as a solid line in panel (a).

In addition, we calculated the magnetic-field dependence of the excitation spectrum. For this case, we perform the powder average using a random field direction with the moments tilted by a fixed angle from their $H = 0$ orientation toward the applied field. We then average this calculated spectrum over 128 random applied field directions. To achieve the correct weighting, each calculated spectrum was normalized by a factor corresponding to the cosine of the angle between the crystallographic ab plane and the direction of the applied field. For each fixed magnitude of magnetic field, we use the $H = 0$ exchange constants and vary the magnitude of the spin-canting angle to compare the calculated spectrum to the measured INS spectrum, using an additive background and overall multiplicative prefactor. The field dependence of the spin-canting angle determined from this method is shown in the inset of Fig. 8. Here, the error bars correspond to an increase in reduced χ^2 by 2.5%. The resulting lineshapes drawn in Fig. 8 are in good agreement with the measured field-dependent spectra. Because of the anisotropy intrinsic to our sample, it is possible that a number of the grains of the powder would be rearranged by the applied magnetic field. To better understand this, we considered the spectrum in Fig. 8 as if the field was solely applied along the c axis of the compound. From examination of the spin-wave scattering intensity, the c-axis component of field is mainly responsible for the shift in the density of magnetic states to lower energy transfers. In this case, the spin canting angle determined as a function of applied field is smaller than the random-field calculation, as is shown in the inset of Fig. 8. For both calculations, we find that the ordered magnetic moments gradually rotate from their $H = 0$ orientation toward the applied magnetic field as a function of the field. The powder nature of the sample does not allow us to easily model the case of a distribution of ordered moment orientations. Considering a linear dependence for the ordered moment direction as a function of field for both models, the shaded region in the inset of Fig. 8 represents the most likely range of canting angles for different orientations of applied field.

3. *Magnetic susceptibility*

The magnetic susceptibility of $[\mathrm{Ni(HF_2)(pyz)_2}]\mathrm{SbF_6}$ exhibits a broad maximum at 16 K associated with the formation of spin correlations along the Ni-FHF-Ni chains as the sample is cooled [27] [Fig. 9(a)]. There is a rapid decrease on reducing T through the ordering transition at 12.2 K and the susceptibility plateaus as T is decreased further. The data for $T \geqslant 10$ K are compared to a simulation of the susceptibility (χ_{sim}) using a 1D chain model [43] of $S = 1$ ions with intrachain exchange J and single-ion anisotropy D. This model is reproduced in the Supplemental Material [30] and can be used to attempt fits of $\chi(T)$ data for powders.

Fixing the powder average g factor to the published value [27], $g = 2.08$, the susceptibility was simulated for parameters in the range $0 \leqslant D \leqslant 30$ K, $5 \leqslant J \leqslant 15$ K, and $10 \leqslant T \leqslant 300$ K ($\Delta T = 1$ K). The quality factor ($R = \sum_i |\chi_{\text{obs},i} - \chi_{\text{sim},i}| / \sum_i \chi_{\text{obs},i}$, where χ_{obs} is the experimentally-determined susceptibility and i runs over all data points for $T \geqslant 10$ K) was computed for each simulated curve. A contour plot of R across the D-J plane [Fig. 9(b)] reveals bands of D and J values that produce χ_{sim} curves providing equally good representations of the data. This insensitivity of the quality factor to a detuning of D and J away from the minimum (white region) indicates that the results of fitting the susceptibility with the model of Ref. [43] should be treated with caution. The parameters D and J are strongly correlated, which likely results from their competing energy scale and the fact that a low-field bulk measurement of the susceptibility, as obtained from a powder sample, cannot differentiate between the effects of the J'/J ratio and single-ion anisotropy for an $S = 1$ chain.

The values of D and J deduced from the mean-field analysis of the magnetization and the more precise results obtained by simulating the INS data [Fig. 9(b), triangles] both fall close to the white band in the contour map, indicating good consistency with the broad temperature dependence of the χ_{obs} data. The high-field magnetization and INS measurements, however, offer a significant advantage over the susceptibility analysis. This results from two key differences in the techniques as compared to the low-field susceptibility measurements: (i) the high-field magnetization is sensitive to the anisotropy of the critical field, and (ii) a local probe such as neutron scattering is sensitive to the local symmetry of the magnetic centers and so a single experiment can constrain both D and J. Thus, the choice of a high-field or local experimental probe was crucial to differentiate the effects of the J'/J ratio and single-ion anisotropy in the magnetic properties of this sample. Furthermore, the simulated susceptibility curve that minimizes R [Fig. 9(a), line] significantly deviates from the measured data in the ordered phase. For temperatures $T \leqslant T_c$, the effects of finite interchain interactions (J') may not be ignored and this further complicates the analysis of the susceptibility at low T. Thus, we find that the local INS probe is necessary to efficiently and precisely determine the full set of parameters (D, J and J') for [Ni(HF$_2$)(pyz)$_2$]SbF$_6$.

C. Calculations and modeling

1. Monte-Carlo simulation of the magnetization

The magnetization of [Ni(HF$_2$)(pyz)$_2$]SbF$_6$ was calculated from a Monte-Carlo energy minimization routine on an 8-spin cluster for 21 orientations of the applied field with respect to the magnetic hard axis of the Ni(II) ions [Fig. 10(a), colored lines]. The critical field was found to be anisotropic, such that a greater applied field is required to saturate the moments as the field orientation is moved away from the easy plane. The resultant powder-average magnetization was determined (thick line, see Eq. (S3) [30]) and compared to the measured magnetization at $T = 0.6$ K (pink line). An overall good agreement of the rounded approach towards saturation for the powdered sample is obtained. Furthermore, the parameters $D = 13.3$ K, $J = 10.3$ K, $J' = 1.43$ K, and $g = 2.11$ yield a good quantitative agreement for the two observed critical fields [Fig. 10(a)].

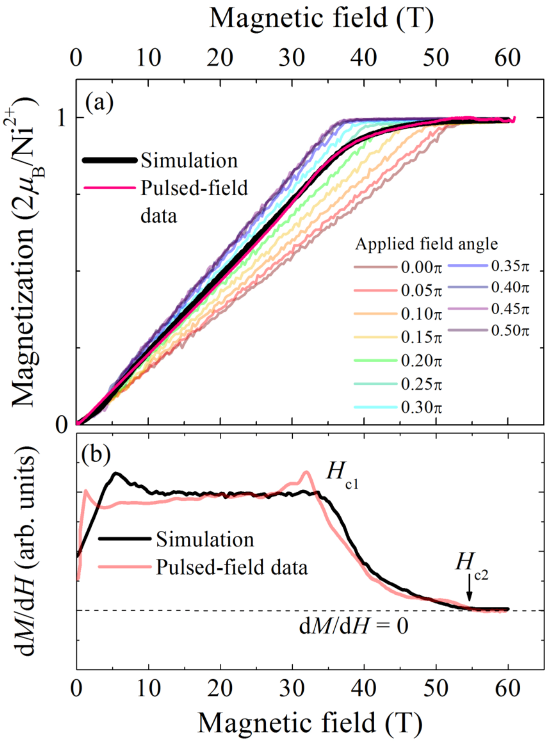

FIG. 10. (a) Simulated magnetization (M) versus field for [Ni(HF$_2$)(pyz)$_2$]SbF$_6$ using a Monte-Carlo energy-minimization routine for an 8-spin cluster governed by Eq. (1) with $D = 13.3$ K, $J = 10.3$ K, $J' = 1.43$ K, and $g = 2.08$. M curves are obtained for 21 orientations of the field with respect to the hard axis (colored lines show the unique angles) and the powder-average M (black line) is determined (see Ref. [30]). Good agreement with the $T = 0.6$ K pulsed-field M data (pink line) is achieved. (b) dM/dH as deduced from the Monte-Carlo simulation (black line) compared with pulsed-field measurements (pink line).

The measured pulsed-field magnetization develops a slight concavity on approaching H_{c1} with increasing field as T is lowered below 8 K [Fig. 10(b)], which leads to a peak in dM/dH at H_{c1}. This behavior is not reproduced by the simulation that employed classical vectors to represent the Ni(II) moments. The discrepancy may be attributed to the development of quantum fluctuations of the $S = 1$ magnetic moments, which result from the Q1D nature of the spin-exchange interactions [44] that act to suppress the magnetization at low temperatures. The data also appear to exhibit a corresponding small hump in dM/dH close to H_{c2}.

At much lower fields (≈2 T), the experimental data show a sharp rise in dM/dH. Though the neutron-scattering data suggest that there is no preferred direction for the moments at low temperatures, this feature could represent a precursor to very low temperature XY symmetry breaking due to rhombic anisotropy or distortion of the exchange energy [11]. Another possible explanation is the presence of antiferromagnetic domains [17] at low magnetic fields and temperatures. The

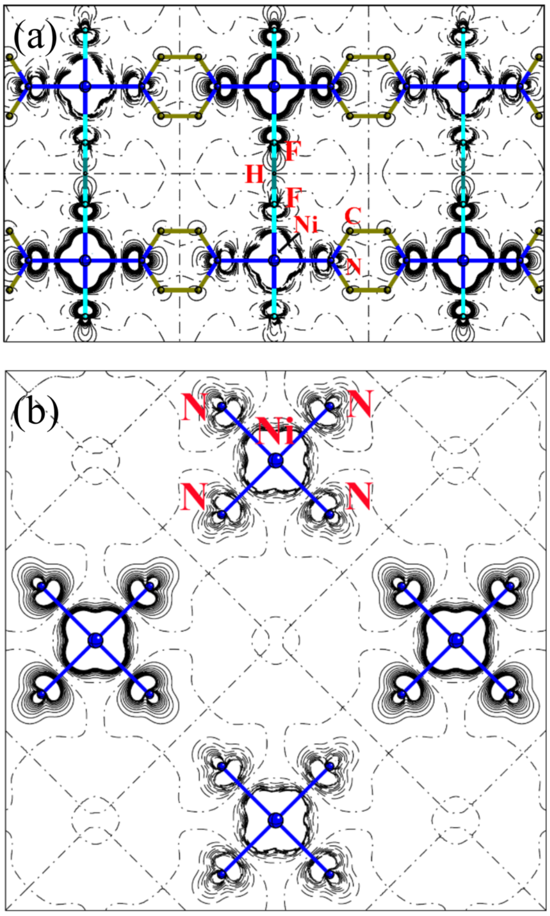

FIG. 11. The electron spin-density distribution in the (a) [110] and (b) [001] planes, calculated for the AFM state (solid and dashed lines represent the excess or defect of α spin-density; contours are drawn with a logarithmic increase). The spin density is delocalized along both ligand types. However, the spin delocalization is essentially quenched along Ni-pyz-Ni because only the σ skeleton is involved. In contrast, the spin delocalization is not disrupted along the Ni-FHF-Ni bridge.

peak close to 5 T in the simulation is unrelated to the low-field peak in the real data; instead, it is an artifact attributable to the finite number of cycles used to determine the ground state spin configuration. This ultimately causes a slight underestimation of the magnetization in this field regime [45].

2. Theoretical spin-density distribution

Periodic DFT calculations on $[\mathrm{Ni(HF_2)(pyz)_2}]\mathrm{SbF_6}$ enabled us to estimate the J and J' exchange constants by calculating the energy of the FM state and of two different AFM states, with spin pairing along the c axis ($\mathrm{AFM_{FHF}}$) or in the ab plane ($\mathrm{AFM_{pyz}}$), as well as the full AFM state with both kinds of pairing (see Ref. [30] for details). The energy difference ΔE between the FM and the $\mathrm{AFM_{FHF}}$ or $\mathrm{AFM_{pyz}}$ states can be used to calculate J or J', respectively, using Eq. (1) and assuming the calculated ΔE to be equivalent to the result of the corresponding Heisenberg Hamiltonian. The primary J can also be obtained from $E(\mathrm{AFM}) - E(\mathrm{AFM_{pyz}})$, whereas J' can be obtained from $E(\mathrm{AFM}) - E(\mathrm{AFM_{FHF}})$. Considering the experimental geometries, both approaches provided $J = 9.2$ K and $J' = 1.8$ K, in good agreement with the model derived from INS. The calculated periodic wave function also enabled mapping of the spin-density distribution in all states. Figure 11 shows the spin-density distribution of the AFM state. For all states (FM or AFM), the Ni atom bears $\approx 1.75e$ of excess spin, where $2e$ is the maximum possible excess spin. The remaining $0.25e$ is delocalized onto all ligands and is responsible for the observed magnetic exchange. Despite $J' \ll J$, the largest spin population lies on the pyrazine N atom ($\approx 0.05e$), whereas only $0.02e$ reside on the F atoms. This is certainly caused by N being a stronger donor than $\mathrm{F^-}$ (in accord with the spectrochemical series). However, because the exchange mechanism through pyrazine is mainly σ type (as shown for some Cu-pyrazine networks) [46] it is not as effective for the magnetic exchange, which explains the smaller J'. The optimal delocalization via the pyrazine bridge would occur through the π electrons which are not significantly involved in the spin density. In fact, population analysis shows that the atomic p orbitals of N and C involved in the pyrazine π system contribute little to the overall spin density. On the other hand, the short F-F distance in the $\mathrm{HF_2^-}$ ligand likely promotes more effective spin delocalization, as evident in Fig. 11(a).

TABLE I. Parameters from Eq. (1) (in Kelvin) as deduced from high-field magnetization data and inelastic neutron-scattering (INS) experiments. For comparison, DFT-computed values are included in the last column. To decompose $n\langle J\rangle$ into individual J and J' contributions from the magnetization data it was necessary to infer an average value of J' from a catalog of related coordination polymers that also contain square $[\mathrm{Ni(pyz)_2}]^{2+}$ motifs (see Table S7 in Ref. [30]).

Parameter (K)	$M(H)$ data	INS data	DFT
D	15 (1)	13.3(1)	
J	9.4(5)	10.4(3)	9.2
J'	0.9(2)	1.4(2)	1.8

III. CONCLUSIONS

$[\mathrm{Ni(HF_2)(pyz)_2}]\mathrm{SbF_6}$ retains tetragonal symmetry for temperatures down to 1.5 K and may be characterized as a Q1D $S = 1$ quantum magnet that exhibits a 3D XY-AFM ground state below 12.2(1) K as determined from high-resolution elastic neutron scattering. The magnetic properties can be described by the Hamiltonian in Eq. (1), with $D = 13.3(1)$ K, $J = 10.4(3)$ K, and $J' = 1.4(2)$ K as determined by INS measurements. We showed that these values are in reasonable agreement with the initial estimates deduced from high-field magnetization studies (see Table I), while low-field bulk thermodynamic probes such as magnetic susceptibility were unable to satisfactorily untangle the effects of the J'/J ratio and single-ion anisotropy. Compared to the previous study [27], the DFT results presented in this work more closely agree with the experimentally derived J and J' parameters.

The predicted [12] phase diagram for easy-plane ($D > 0$) Q1D spin-1 systems is shown in Fig. 12. The phase boundaries, as deduced from QMC calculations, separate regions of XY-AFM order from the disordered quantum paramagnetic and Haldane phases; the three phases converge [12] at the quantum critical point $D/J = 0.97$. The relative position

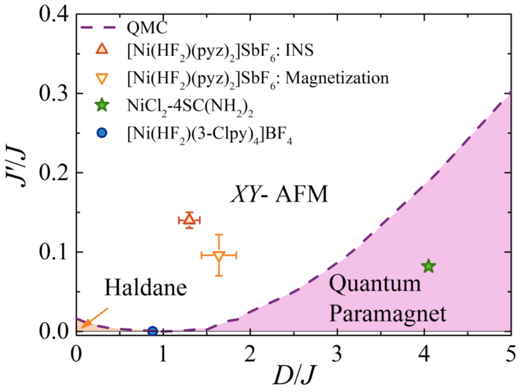

FIG. 12. Phase diagram of $S = 1$ Q1D materials as a function of intrachain exchange (J), interchain interaction (J'), and single-ion anisotropy (D). The phase boundaries are the results of quantum Monte-Carlo calculations [12]. The position of [Ni(HF$_2$)(pyz)$_2$]SbF$_6$ as determined from both pulsed-field magnetization and INS (triangles) predicts the material to have an antiferromagnetic XY-ordered ground state. The positions of the quantum paramagnet [7] NiCl$_2$-4SC(NH$_2$)$_2$ (star) and Haldane-chain system [11] [Ni(HF$_2$)(3-Clpy)$_4$]BF$_4$ (circle) are included for comparison.

of [Ni(HF$_2$)(pyz)$_2$]SbF$_6$ is indicated on the phase diagram using both the precise J'/J and D/J ratios from INS and those estimated from a mean-field analysis of the critical fields observed in pulsed-field magnetization. Both estimates predict [Ni(HF$_2$)(pyz)$_2$]SbF$_6$ to exhibit an XY-AFM ground state, though only INS independently determined all three parameters needed to validate this prediction. The lack of a gapped ground state is in full agreement with both the field-dependent heat capacity, which showed clear evidence of a transition to an AFM ground state, and the refined magnetic structure from elastic neutron scattering in zero field.

Prior to the current work, only one real material had been identified as being close to the quantum critical point, $D/J \approx 1$. This region of the phase diagram has attracted wide theoretical and numerical attention [11]; besides unusual phenomena that may accompany the critical point, it separates two topologically distinct gapped phases with different parity. [Ni(HF$_2$)(pyz)$_2$]SbF$_6$ is an excellent candidate to study this region; molecular architecture (e.g., isotopic substitution or variation of the counter ion), pressure, or (especially) uniaxial stress can be used to fine tune the parameters D, J, and J' to explore the phase diagram and further test the predictions of QMC simulations for Q1D $S = 1$ systems. Pressure studies along a line $D/J =$ constant traversing from XY antiferromagnet to quantum paramagnet would yield the intriguing possibility of tracing lines of quantum critical points between the three phases.

While there is no substitute for the detailed study of single crystals, the success of this work on powder samples demonstrates the complementary capabilities of the micro- and macroscopic probes involved. More specifically, the experimental sequence is as follows: (i) microcrystal synchrotron x-ray diffraction determines the crystal structure; (ii) using this structure, an analysis of the powder-elastic neutron diffraction establishes the magnetic ground state and charts the evolution of the ordered moment as a function of temperature; (iii) from this ground-state magnetic structure, an analysis of the powder-inelastic neutron scattering determines the magnetic exchange and anisotropy parameters; (iv) an independent estimate of these parameters is possible via a careful analysis of the high-field powder magnetometry data and is found to be in good agreement with the results of the neutron scattering; (v) the field-temperature phase diagram is mapped out using high-field-magnetization and heat-capacity measurements. Having established the applicability of the methodology, we are currently applying this experimental protocol to other $S = 1$ materials.

ACKNOWLEDGMENTS

The work at EWU was supported by the National Science Foundation (NSF) under Grant No. DMR-1306158 and by the National Institute of Standards and Technology (NIST) Cooperative Agreement 70NANB15H262. ChemMatCARS Sector 15 is principally supported by the Divisions of Chemistry (CHE), NSF, under Grant No. CHE-1346572. Use of the Advanced Photon Source, an Office of Science User Facility operated for the U.S. Department of Energy (DoE) Office of Science by Argonne National Laboratory, was supported by the U.S. DoE under Contract No. DE-AC02-06CH11357. We acknowledge the support of NIST, U.S. Department of Commerce (DoC), in providing their neutron research facilities used in this work; identification of any commercial product or trade name does not imply endorsement or recommendation by NIST. Work performed at the National High Magnetic Field Laboratory, USA, was supported by NSF Cooperative Agreement DMR-1157490, the State of Florida, U.S. DoE, and through the DoE Basic Energy Science Field Work Project Science in 100 T. M.B.S. was supported by the Scientific User Facilities Division, Office of Basic Energy Sciences, U.S. Department of Energy. We gratefully acknowledge the ISIS-RAL facility for the provision of beamtime. J.B. thanks EPSRC for financial support. P.A.G. acknowledges that this project has received funding from the European Research Council (ERC) under the European Union's Horizon 2020 research and innovation programme (Grant agreement No. 681260). Research at the University of Bern was funded by the Swiss NSF (project 160157). J.S. acknowledges a Visiting Professorship from the University of Oxford that enabled some of the experiments reported in this paper. Data presented in this paper resulting from the UK effort will be made available at http://wrap.warwick.ac.uk/87183.

---

[1] J. M. Kosterlitz and D. J. Thouless, J. Phys. C: Solid State Phys. **5**, L124 (1972).
[2] J. M. Kosterlitz and D. J. Thouless, J. Phys. C: Solid State Phys. **6**, 1181 (1973).
[3] F. D. M. Haldane, Phys. Lett. A **93**, 464 (1983).
[4] F. D. M. Haldane, Phys. Rev. Lett. **50**, 1153 (1983).
[5] The Nobel Prize in Physics 2016 Advanced Information, Nobelprize.org., Nobel Media AB 2014, http://www.nobelprize.org/nobel_prizes/physics/laureates/2016/advanced.html.

[6] A. Paduan-Filho,X. Gratens, and N. F. Oliveira, Phys. Rev. B **69**, 020405R (2004).

[7] V. S. Zapf, D. Zocco, B. R. Hansen, M. Jaime, N. Harrison, C. D. Batista, M. Kenzelmann, C. Niedermayer, A. Lacerda, and A. Paduan-Filho, Phys. Rev. Lett. **96**, 077204 (2006).

[8] L. Yin, J.-S. Xia, V. S. Zapf, N. S. Sullivan, and A. Paduan-Filho, Phys. Rev. Lett. **101**, 187205 (2008).

[9] J. P. Renard, M. Verdaguer, L. P. Regnault, W. A. C. Erkelens, J. Rossat-Mignod, and W. G. Stirling, Europhys. Lett. **3**, 945 (1987).

[10] J. L. Manson, A. G. Baldwin, B. L. Scott, J. Bendix, R. E. Del Sesto, P. A. Goddard, Y. Kohama, H. E. Tran, S. Ghannadzadeh, J. Singleton, T. Lancaster, J. S. Möller, S. J. Blundell, F. L. Pratt, V. S. Zapf, J. Kang, C. Lee, M.-H. Whangbo, and C. Baines, Inorg. Chem. **51**, 7520 (2012).

[11] J.-S. Xia, A. Ozarowski, P. M. Spurgeon, A. C. Baldwin, J. L. Manson, and M. W. Meisel, arXiv:1409.5971.

[12] K. Wierschem and P. Sengupta, Mod. Phys. Lett. B **28**, 1430017 (2014) and refs. therein.

[13] S. Sachdev and B. Keimer, Phys. Today **64**, 29 (2011).

[14] R. Boča, Coord. Chem. Rev. **248**, 757 (2004).

[15] J. L. Manson, A. Ozarowski, S. H. Lapidus, J. A. Villa, A. Sarkar, S. Saeidi, and M. W. Meisel (unpublished).

[16] W. J. Blackmore *et al.* (in preparation).

[17] *Neutron Scattering from Magnetic Materials*, edited by T. Chatterji (Elsevier Science, London, 2006).

[18] O. Pieper, T. Guidi, S. Carretta, J. van Slageren, F. El Hallak, B. Lake, P. Santini, G. Amoretti, H. Mutka, M. Koza, M. Russina, A. Schnegg, C. J. Milios, E. K. Brechin, A. Julià, and J. Tejada, Phys. Rev. B **81**, 174420 (2010).

[19] H. Andres, R. Basler, H.-U. Güdel, G. Aromi, C. Christou, H. Büttner, and B. Rufflé, J. Am. Chem. Soc. **122**, 12469 (2000).

[20] A. B. Boeer, A.-L. Barra, L. F. Chibotaru, D. Collison, E. J. L. McInnes, R. A. Mole, G. G. Simeoni, G. A. Timco, L. Ungur, T. Unruh, and R. E. P. Winpenny, Angew. Chem., Int. Ed. **50**, 4007 (2011).

[21] K. G. Alley, R. Bircher, O. Waldmann, S. T. Ochsenbein, H.-U. Güdel, B. Moubaraki, K. S. Murray, F. Fernandez-Alonso, B. F. Abrahams, and C. Boskovic, Inorg. Chem. **45**, 8950 (2006).

[22] J. M. Clemente-Juan, E. Coronado, A. Gaita-Ariño, C. Saiz-Giménez, H.-U. Güdel, A. Sieber, R. Bircher, and H. Mutka, Inorg. Chem. **44**, 3389 (2005).

[23] J. L. Manson, Q.-Z. Huang, C. M. Brown, J. W. Lynn, M. B. Stone, J. Singleton, and F. Xiao, Inorg. Chem. **54**, 11897 (2015).

[24] B. J. Houghton and R. J. Deeth, Eur. J. Inorg. Chem. **2014**, 4573 (2014).

[25] A. J. Cohen, P. Mori-Sanchez, and W. Yang, Chem. Rev. **112**, 289 (2012).

[26] F. Neese, Coord. Chem. Rev. **253**, 526 (2009).

[27] J. L. Manson, S. H. Lapidus, P. W. Stephens, P. K. Peterson, K. E. Carreiro, H. I. Southerland, T. Lancaster, S. J. Blundell, A. J. Steele, P. A. Goddard, F. L. Pratt, J. Singleton, Y. Kohama, R. D. McDonald, R. E. Del Sesto, N. A. Smith, J. Bendix, S. A. Zvyagin, J. Kang, C. Lee, M.-H. Whangbo, V. S. Zapf, and A. Plonczak, Inorg. Chem. **50**, 5990 (2011).

[28] K. R. O'Neal, B. S. Holinsworth, Z. Chen, P. K. Peterson, K. E. Carreiro, C. Lee, J. L. Manson, M.-H. Whangbo, Z. Li, Z. Liu, and J. L. Musfeldt, Inorg. Chem. **55**, 12172 (2016).

[29] S. Toth and B. Lake, J. Phys.: Condens. Matter **27**, 166002 (2015).

[30] See Supplemental Material at http://link.aps.org/supplemental/10.1103/PhysRevB.95.134435 for additional information.

[31] J. Liu, P. A. Goddard, J. Singleton, J. Brambleby, F. Foronda, J. S. Möller, Y. Kohama, S. Ghannadzadeh, A. Ardavan, S. J. Blundell, T. Lancaster, F. Xiao, R. C. Williams, F. L. Pratt, P. J. Baker, K. Wierschem, S. H. Lapidus, K. H. Stone, P. W. Stephens, J. Bendix, M. R. Lees, T. J. Woods, K. E. Carreiro, H. E. Tran, C. J. Villa, and J. L. Manson, Inorg. Chem. **55**, 3515 (2016), and unpublished results.

[32] F. Lloret, M. Julve, J. Cano, and G. De Munno, Mol. Cryst. Liq. Cryst. **334**, 569 (1999).

[33] J. Rodriguez-Carvajal, Physica (Amsterdam) **192**, 55 (1993).

[34] http://stokes.byu.edu/iso/isodistort.php.

[35] J. Brambleby, P. A. Goddard, R. D. Johnson, J. Liu, D. Kaminski, A. Ardavan, A. J. Steele, S. J. Blundell, T. Lancaster, P. Manuel, P. J. Baker, J. Singleton, S. Schwalbe, P. M. Spurgeon, H. E. Tran, P. K. Peterson, J. F. Corbey, and J. L. Manson, Phys. Rev. B **92**, 134406 (2015).

[36] We refer to the ordering temperature as T_c, rather than T_N, as our system is not a conventional Néel antiferromagnet.

[37] R. F. Wielinga, *Prog. Low Temp. Phys.* Vol. VI, p. 333 (North Holland, Amsterdam, 1970).

[38] J. L. Manson, J. A. Schlueter, K. A. Funk. H. I. Southerland, B. Twamley, T. Lancaster, S. J. Blundell, P. J. Baker, F. L. Pratt, J. Singleton, R. D. McDonald, P. A. Goddard, P. Sengupta, C. D. Batista, L. Ding, C. Lee, M.-H. Whangbo, I. Franke, S. Cox, C. Baines, and D. Trial, J. Am. Chem. Soc. **131**, 6733 (2009).

[39] M. Sorai, M. Nakano, and Y. Miyazaki, Chem. Rev. **106**, 976 (2006).

[40] W. J. A. Blackmore, J. Brambleby, P. A. Goddard, M. Healey, B. Slater, J. Singleton, A. Ozarowski, J. A. Schlueter, S. H. Lapidus, J. A. Villa, D. Y. Villa, and J. L. Manson (unpublished).

[41] M. B. Stone, G. Ehlers, and G. Granroth, Phys. Rev. B **88**, 104413 (2013).

[42] M. B. Stone, M. D. Lumsden, Y. Qiu, E. C. Samulon, C. D. Batista, and I. R. Fisher, Phys. Rev. B **77**, 134406 (2008).

[43] J. J. Borrás-Almenar, E. Coronado, J. Curely, and R. Georges, Inorg. Chem. **34**, 2699 (1995).

[44] K. Wierschem, P. Sengupta, J. Phys.: Conf. Ser. **400**, 032112 (2012).

[45] At low fields, where the number of degenerate ground states in the uniaxial system is greatest, running a finite length Monte-Carlo Markov chain simulation to iterate an ensemble of spins towards their ground state configuration can lead to a small proportion of the spins ending up perturbed from their lowest energy orientation. Through averaging the final magnetization over many repeated simulations performed in this manner, this can lead to an underestimation of the magnetization and the slight kink in M versus H as found in the simulated traces.

[46] L. H. R. Dos Santos, A. Lanza, A. M. Barton, J. Brambleby, W. J. A. Blackmore, P. A. Goddard, F. Xiao, R. C. Williams, T. Lancaster, F. L. Pratt, S. J. Blundell, J. Singleton, J. L. Manson, and P. Macchi, J. Am. Chem. Soc. **138**, 2280 (2016).